

PAPER • OPEN ACCESS

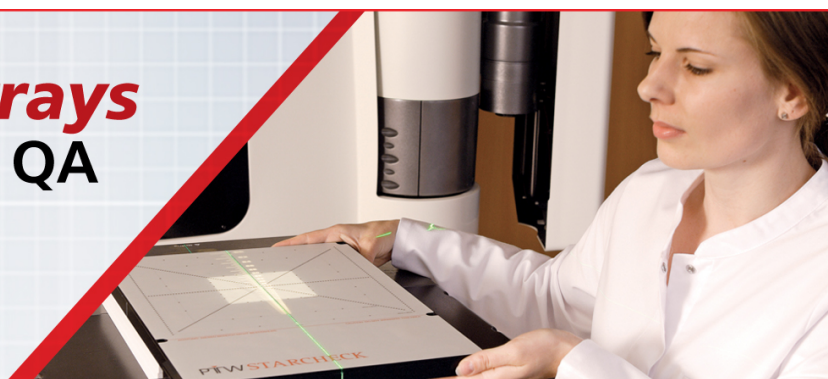
Optimizing robot motion for robotic ultrasound-guided radiation therapy

To cite this article: Matthias Schlüter *et al* 2019 *Phys. Med. Biol.* **64** 195012

View the [article online](#) for updates and enhancements.

STARCHECK® Arrays
Fast, Precise LINAC QA

PTW
THE
DOSIMETRY
COMPANY



OPEN ACCESS



CrossMark

RECEIVED

22 December 2018

REVISED

1 August 2019

ACCEPTED FOR PUBLICATION

16 August 2019

PUBLISHED

4 October 2019

Original content from this work may be used under the terms of the [Creative Commons Attribution 3.0 licence](https://creativecommons.org/licenses/by/3.0/).

Any further distribution of this work must maintain attribution to the author(s) and the title of the work, journal citation and DOI.



PAPER

Optimizing robot motion for robotic ultrasound-guided radiation therapy

Matthias Schlüter¹, Christoph Fürweger^{2,3} and Alexander Schläefer¹¹ Institute of Medical Technology, Hamburg University of Technology, Hamburg, Germany² Europäisches Cyberknife Zentrum München-Großhadern, Munich, Germany³ Department of Stereotaxy and Functional Neurosurgery, University of Cologne, Faculty of Medicine and University Hospital Cologne, Cologne, GermanyE-mail: matthias.schlueter@tuhh.de and schlaefer@tuhh.de**Keywords:** radiation therapy, robotic ultrasound, path planning, treatment planning, image guidance

Abstract

An important aspect of robotic radiation therapy is active compensation of target motion. Recently, ultrasound has been proposed to obtain real-time volumetric images of abdominal organ motion. One approach to realize flexible probe placement throughout the treatment fraction is based on a robotic arm holding the ultrasound probe. However, the probe and the robot holding it may obstruct some of the beams with a potentially adverse effect on the plan quality. This can be mitigated by using a kinematically redundant robot, which allows maintaining a steady pose of the ultrasound probe while moving its elbow in order to minimize beam blocking. Ultimately, the motion of both the beam source carrying and the ultrasound probe holding robot contributes to the overall treatment time, i.e. beam delivery and robot motion. We propose an approach to optimize the motion and coordination of both robots based on a generalized traveling salesman problem. Furthermore, we study an application of the model to a prostate treatment scenario. Because the underlying optimization problem is hard, we compare results from a state-of-the-art heuristic solver and an approximation scheme with low computational effort. Our results show that integration of the robot holding the ultrasound probe is feasible with acceptable overhead in overall treatment time. For clinically realistic velocities of the robots, the overhead is less than 4% which is a small cost for the added benefit of continuous, volumetric, and non-ionizing tracking of organ motion over periodic x-ray-based tracking.

1. Introduction

Stereotatic body radiation therapy (SBRT) is a non-invasive approach to cancer treatment. It uses dose distributions which are designed to cover the target structures (planning target volume, PTV) very well while at the same time sparing other critical structures (organs at risk, OARs). In the case of prostate cancer, the intention is to reduce the dose in bladder and rectum, for example.

The flexibility of robotic radiation therapy to deliver beams from a wide range of positions around the patient can help shaping very conformal dose distributions with steep gradients towards critical structures (Hossain *et al* 2010, Schläefer *et al* 2013). Another important and interesting aspect of robotic radiation therapy is active compensation of target motion. By detecting the motion of the target and moving the treatment beams accordingly, the adverse effect of organ motion can be mitigated and hence the safety margins accounting for organ motion can be reduced (Beltran *et al* 2008, Ricotti *et al* 2018). So far, approaches based on x-ray imaging (Krauss *et al* 2012, Nguyen *et al* 2017) and surrogate markers (Dürichen *et al* 2014, Antoni *et al* 2016) have dominated. Typically, the target region is defined by fiducial markers implanted before treatment. For some targets in the thorax, direct localization is feasible (Jung *et al* 2015, Yang *et al* 2017). However, given its ionizing nature, x-ray imaging is typically not used for continuous motion tracking. Moreover, this approach does not extend to targets in the abdomen, which are often not clearly visible in x-ray images.

In contrast, volumetric ultrasound (US) presents a non-ionizing image modality with high spatial and temporal resolution. Recently, a number of approaches to use ultrasound for motion compensated treatments have been proposed (Schwaab *et al* 2014, Western *et al* 2015, Schlosser and Hristov 2016, Camps *et al* 2018). Ipsen *et al* (2016) demonstrated 4D tracking for MLC-based motion compensation by acquiring US volumes with $0.3 \times 0.8 \times 1.6 \text{ mm}^3$ resolution and sizes from $17 \times 14 \times 45 \text{ mm}^3$ at 250 Hz volume rate to $68 \times 105 \times 170 \text{ mm}^3$ at 17.8 Hz. Note that the dimension of the volumes will cover typical target motion, e.g. of the prostate. Moreover, even if motion exceeding this range occurred, the tracking would detect this and similar strategies as in current motion compensated treatments could be employed, e.g. emergency stop and re-setup. Tracking algorithms for both 2D and 3D ultrasound images have been evaluated and showed that this modality can be suitable for tracking of targets like the liver or the prostate (O'Shea *et al* 2014, De Luca *et al* 2018).

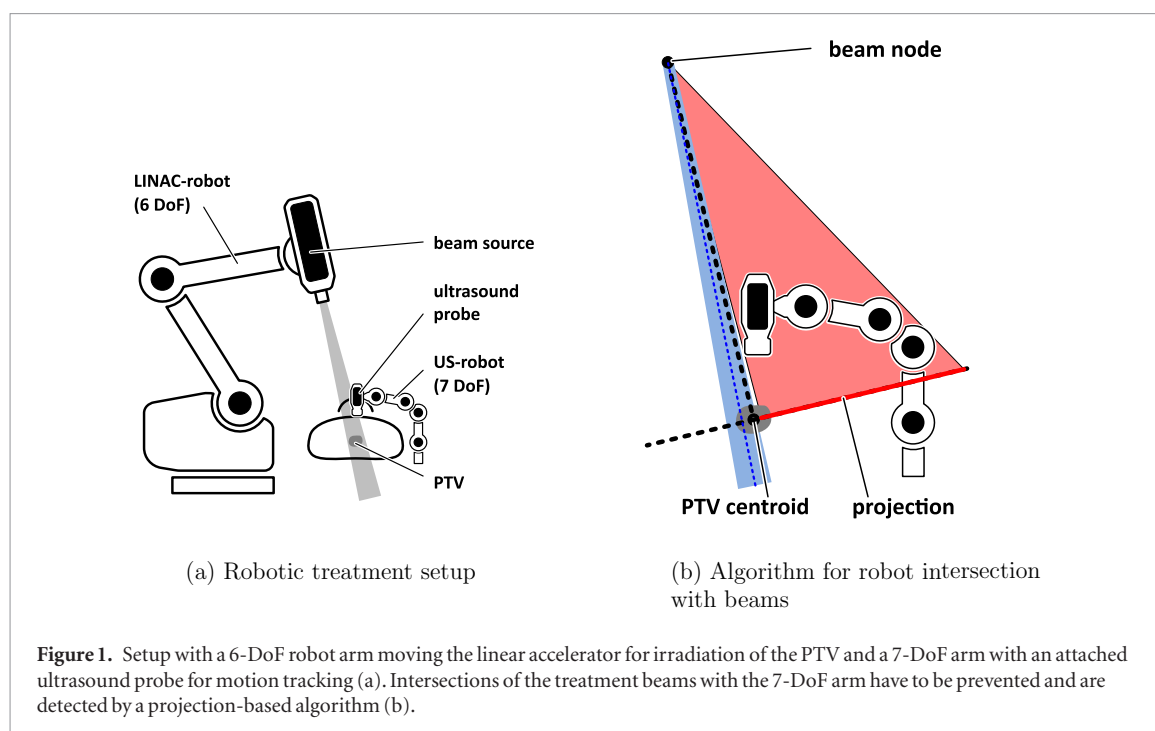
While it has been demonstrated that 4D ultrasound can be a viable alternative to obtain real-time images of the abdominal anatomy, a remaining challenge is its integration with the treatment systems. Particularly, the ultrasound probe needs to be positioned at the patient such that high quality imaging of the target region is feasible throughout the treatment. This can be realized by using a robotic arm holding the ultrasound probe (Priester *et al* 2013, Bell *et al* 2014, Şen *et al* 2017). Different approaches have been considered to integrate ultrasound imaging with radiation therapy, where beams should not pass through the ultrasound probe or the robot and therefore some beams may be effectively blocked. Elekta proposed a setup where the transducer is placed at the perineum (Abramowitz *et al* 2012, Li *et al* 2015). However, this is primarily limited to imaging the prostate. Also the use of specialized robot systems has been studied (Schlosser *et al* 2016). Nevertheless, there will always be a residual blocking of beam directions by the probe itself (Bazalova-Carter *et al* 2015), because ultrasound imaging requires direct contact of the probe with the patient close to the target structure. For this reason, a special radiolucent ultrasound system has been proposed which also aims to reduce distortion of computed tomography (CT) images while the probe is present (Schlosser and Hristov 2016). The latter aspect is important because the pressure of the probe induces deformations and a planning CT without the probe does not reflect the actual geometry during US imaging. Therefore, workflows for reproducible probe placement have been developed (Bell *et al* 2014, Şen *et al* 2017).

It has also been demonstrated that the freedom in beam delivery of the robotic CyberKnife (Accuray Inc., United States) combined with an optimized configuration of a robot carrying the ultrasound probe will largely compensate for possible adverse effects to the treatment plan quality (Gerlach *et al* 2017a, 2017b). Considering the expected beam blocking during treatment planning it is possible to determine a set of treatment beams and a configuration for the robot carrying the ultrasound probe such that the change in plan quality compared to a setup without ultrasound is very small. Recently, also automatic approaches to determine a robot setup with minimum impact on the plan quality have been proposed (Schlüter *et al* 2019). Particularly, employing a kinematically redundant robot like the light-weight robot iiwa (KUKA Roboter GmbH, Germany) to carry the ultrasound probe can further reduce the beam blocking. Its seven degrees of freedom (DoF) allow to continuously change the orientation of the robot's elbow while maintaining the same pose of the end-effector. Thereby, the robot is able to maintain ultrasound transducer contact and provide steady imaging throughout the beam delivery, even when it changes its configuration. This is interesting, as beams blocked by the elbow in one configuration may not be blocked in another configuration and changing configurations would not affect the ultrasound imaging. It has been shown that this extra flexibility can indeed improve the dosimetrical plan quality further (Gerlach *et al* 2017a, Schlüter *et al* 2019) and it has been demonstrated how the calibrations between the different systems and coordinate frames can be realized (Gerlach *et al* 2017a). For the inverse kinematic, this elbow rotation due to the additional degree of freedom can be parametrized by a continuous angle we call LIFT (Kuhleermann *et al* 2016).

However, while the dose distribution is the key determinant for plan quality, delivery time contributes to treatment quality, workflow, and patient experience. The potential need to wait for the ultrasound robot to change its configuration before continuing beam delivery from a certain direction will take time and prolong the treatment. The problem to optimize the sequence of beam source motions during beam delivery can be modeled as a traveling salesman problem (TSP) (Kearney *et al* 2017). While in general the TSP is known to be hard, we first demonstrate that the particular instances resulting from the CyberKnife setup can be efficiently solved with state-of-the-art methods. Yet, when including the configuration changes of the ultrasound robot, the problem becomes more difficult. Second, we derive a generalized TSP (GTSP) model for the two-robot setup. We compare two approaches to solve this problem. Finally, we provide an analysis of the effect of the optimization for different assumptions regarding the robots' velocity settings.

2. Material and methods

In this section, we first describe our general treatment planning setup. We then introduce the robots considered in our US-guided robotic radiation-therapy scenario, namely the robot carrying the linear accelerator (LINAC-robot) and the robot carrying the ultrasound probe (US-robot) as sketched in figure 1(a). Furthermore, we



develop models to coordinate and optimize robot motion and beam delivery. We describe two approaches to solve the underlying optimization problems and present a case study to evaluate our methods.

2.1. Treatment plan optimization

In robotic radiation therapy, beams are delivered from a finite set of points roughly distributed over a hemisphere around the patient. The points are often called nodes. At each node, beams with different orientation and shape can be delivered. Different collimators shaping the aperture are in use with the CyberKnife, including cylinder collimators, an IRIS collimator (Echner *et al* 2009), and a multi-leaf collimator (MLC) (Fürweger *et al* 2016). However, for our purpose the shape of the beams is not important, as the blocking of complete or partial beams mainly depends on the overall beam direction and the configuration of the US-robot. For simplicity we consider circular beams of different diameter and orientation, i.e. starting at one node and passing through the PTV. Furthermore, given the infinite number of possible beams we adopt the typical approach to generate a set of candidate beams heuristically. Given the set of candidate beams the beam activation times or beam weights can be obtained by inverse planning (Schlaefer and Schweikard 2008).

In our scenario, some of the beams might be blocked by the US-robot, i.e. they would pass through either the robot or the ultrasound probe. For each node and each US-robot configuration it is possible to compute the projection of robot and transducer into a plane orthogonal to a line connecting the node and the centroid of the PTV. Using a distance transform on the projection and accounting for uncertainties we can establish whether a beam overlaps with the projection and therefore is blocked (Gerlach *et al* 2017a). Figure 1(b) summarizes this approach. Considering the set of suitable configurations of the US-robot, we discard and re-sample beams blocked in all of these configurations. Hence, we eventually arrive at the desired number of candidate beams which are feasible in at least one configuration of the US-robot.

Our actual inverse planning uses a step-wise multi-criteria approach based on linear programming (Schlaefer and Schweikard 2008). Note that there are two key advantages of this approach in the context of a low level analysis of treatment planning. First, the fixed bounds on all upper dose bounds prevent any side effects, e.g. small violations of the dose constraints for OAR. Second, having access to the actual objective value from the optimization underlying the inverse planning we can compare different algorithms without confounding by effects due to discretization and interpolation.

2.2. Robot parameters

Any motion of the robots carrying the linear accelerator and the ultrasound probe is limited by their respective joint speeds. We consider kinematic parameters of a large articulated arm (KR 300 R2500 ultra, KUKA Roboter GmbH, Germany) for the LINAC-robot. This robot represents a standard serial kinematic chain with six DoF. For the US-robot we consider a light-weight device with seven DoFs (LBR iiwa, KUKA Roboter GmbH, Germany). The additional joint results in a kinematic redundancy allowing for rotation of the elbow while maintaining the end-effector pose. While our methods work for any ultrasound-probe shape, we consider an actual 4D

ultrasound probe (GE 3V, General Electric, USA), which is a 2D matrix array probe, for our experiments. The setup with both robots is illustrated in figure 1(a). The maximum joint velocities of the KR range from 101 to 122 deg s⁻¹ for the first five joints and is 175 deg s⁻¹ for the last. For the LBR iiwa, the first three joints are limited to 98–100 deg s⁻¹, the fourth to 130 deg s⁻¹, the fifth to 140 deg s⁻¹, and the last two joints to 180 deg s⁻¹. However, considering the payload and safety concerns in a clinical setting, much lower velocities will be used in practice (McGuinness *et al* 2015). We study velocities ranging from 1% to 10% of the maximum values.

Following the derivation of an analytic inverse kinematic by (Kuhlemann *et al* 2016), different configurations of the US-robot can be parametrized by a continuous angle which we call LIFT. By varying this LIFT angle during the treatment, it is possible to reduce the number of blocked beams, i.e. beams blocked in one elbow configurations may be unblocked in another elbow configuration.

2.2.1. Beam delivery without ultrasound robot

After solving the inverse planning problem, we obtain a set B of N treatment beams $b_i, i = 1, \dots, N$ with non-zero weight which have to be delivered by the linear accelerator. Hence, the LINAC-robot has to move to all nodes where treatment beams start. Multiple beams may start at each node and small changes in the beam orientation also require some robot motion. The order in which the CyberKnife delivers the beams determines the time required for robot motion. For example, it is typically less efficient to visit a different node after each delivered beam compared to first delivering all beams from one node before moving to the next node. To minimize the overall treatment time, we are therefore interested in a sequence of beams which minimizes the total robot motion time.

The problem of finding such a sequence of beams can be modeled as a TSP. Consider a complete graph $G = (V, E)$ with a set of vertices V which are connected by a set of edges $E = \{(v_i, v_j) : v_i, v_j \in V\}$. We assign a non-negative weight

$$d(v_i, v_j) = d_{ij} \geq 0 \quad (1)$$

to each edge $(v_i, v_j) \in E$, which represents the distance or costs for traveling between the two vertices. We use symmetric weights, i.e. $d_{ij} = d_{ji}$ for all i, j , and further set $d_{ii} = 0$. A path in such a graph is a sequence of distinct vertices. If only the first and last vertex in a sequence are identical, it is called a cycle. The TSP now asks for an optimal tour, which is a cycle containing each vertex of the graph. Optimality is defined in terms of minimizing the sum of costs d_{ij} of the involved edges in the tour, i.e. the edges which directly connect the sequent vertices. Given N vertices, there are in total not $N!$ but $(N-1)!/2$ different tours, because a tour does neither have a defined start (factor of N) nor a defined direction in the case of symmetric costs (factor of 2). For example, the tours described by (v_1, v_2, v_3, v_1) , (v_2, v_3, v_1, v_2) , and (v_1, v_3, v_2, v_1) are all equivalent.

In our scenario, each treatment beam b_i is related to a vertex such that

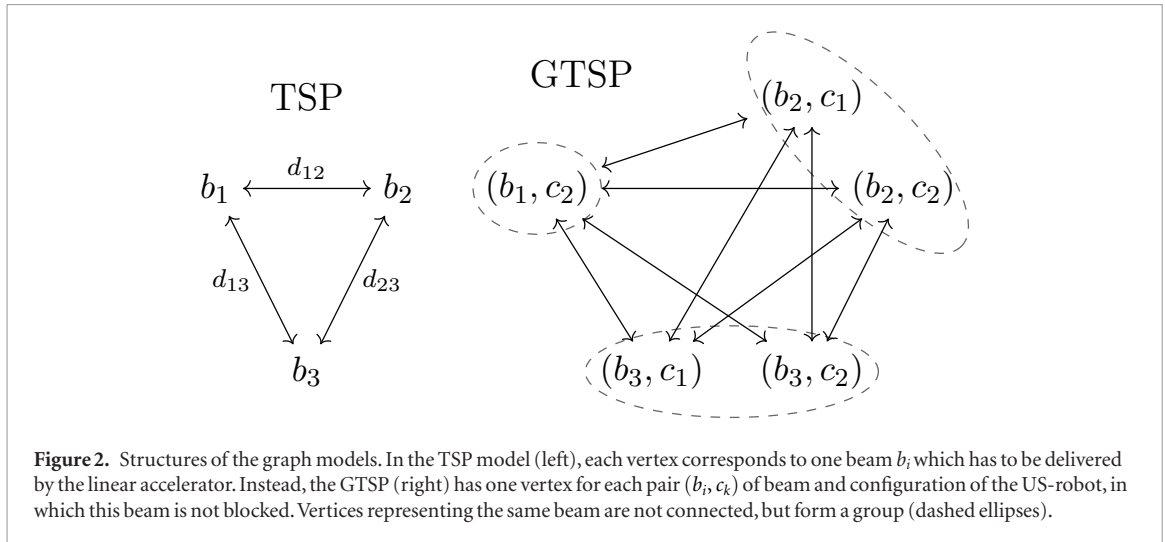
$$V_{\text{TSP}} = \{b_i : i \in \{1, \dots, N\}\} \quad (2)$$

is the set of vertices to be visited and the cost for traveling between two vertices is the time needed for changing the end-effector pose of the LINAC-robot accordingly. We estimate this time as

$$d_{ij} = t_{\text{LA}}(b_i, b_j) = \max_{g \in \{1, \dots, 6\}} \frac{|\theta_g^i - \theta_g^j|}{\lambda_{\text{LA}} s_g^{\text{LA}}}, \quad (3)$$

where θ_g^i is the angle of the g th joint, which is calculated from inverse kinematics for realizing beam b_i . The differences between the angles are calculated by using the identity $\theta = \theta + n \cdot 2\pi, n \in \mathbb{Z}$, and are wrapped to the half-open interval $[-\pi, \pi)$. The denominator is the velocity of the joint, which we assume to be a fraction $\lambda_{\text{LA}} \in (0, 1]$ of its maximum velocity s_g^{LA} . Note that the total treatment time would include beam delivery. However, as the beam weights result from inverse planning they are fixed. Also, the time needed to change the effective diameter of the IRIS collimator is neglected as it is not related to the robot motion and could be realized concurrently.

The solution of a TSP is an optimal tour, i.e. the first and the last visited vertex are equal. In terms of our radiotherapy scenario, this means that the LINAC-robot eventually moves back to its initial pose although the related beam has already been delivered. This is neither necessary nor intuitive. Thus, we search for a path containing all vertices exactly once rather than for a cycle. Such a path is called a Hamiltonian path resulting in a shortest Hamiltonian path problem (HPP). Yet, we can transform the HPP into an equivalent TSP by adding an artificial vertex connected to all other vertices with zero costs. In the resulting optimal tour, the successor and predecessor of this artificial node are the first and last node in the optimal Hamiltonian path, respectively. For example, an optimal tour $(v_1, v_2, \dots, v_5, v^a, v_6, \dots, v_N, v_1)$ with actual vertices $v_i, i = 1, \dots, N$, and artificial vertex v^a is converted to the optimal Hamiltonian path $(v_6, \dots, v_N, v_1, v_2, \dots, v_5)$ only containing the N actual vertices. The size of the solution space is $N!/2$ for an HPP with N vertices and thus a factor of N larger than for a TSP, because it has a defined start.



The direction is still not relevant due to the symmetric costs. For simplicity, we will subsequently describe the TSP models, but all results are computed for the associated HPP.

2.2.2. Beam delivery including the robotic ultrasound

The kinematic redundancy of the US-robot allows delivering beams by moving the elbow such that the beams are no longer blocked. Such a motion will take time, i.e. the problem to optimize the treatment delivery needs to include the motion of both the LINAC-robot and the US-robot. Note that both robots may move concurrently. We consider M configurations $c_k, k = 1, \dots, M$, of the US-robot such that each beam is feasible, i.e. not blocked, in at least one configuration. We map each beam b_j to its set F_j of feasible configurations

$$F(b_j) = F_j = \{c_k : b_j \text{ feasible in } c_k \text{ and } k \in \{1, \dots, M\}\}. \quad (4)$$

We create a new model where for each beam b_j all pairs $(b_j, c_k), c_k \in F_j$, are added as vertices. Therefore, the number of vertices increases from N to up to NM . Assuming that both robots do not change their configurations during beam delivery we model the cost for robot motion by extending equation (3) to

$$\bar{d}_{ijkl} = t((b_i, c_k), (b_j, c_l)) = \max\{t_{LA}(b_i, b_j), t_{US}(c_k, c_l)\}, \quad (5)$$

where $t_{US}(c_k, c_l)$ is calculated similarly to $t_{LA}(b_i, b_j)$ but with a 7th joint as

$$t_{US}(c_k, c_l) = \max_{g \in \{1, \dots, 7\}} \frac{|\theta_g^k - \theta_g^l|}{\lambda_{US} s_g^{US}}. \quad (6)$$

Solving this problem as an ordinary TSP would result in a sequence including all pairs (b_j, c_k) , i.e. each feasible US-robot configuration would be considered for each beam. To identify a sequence containing each beam just once we need to solve the generalized TSP, also known as set TSP or group TSP (Noon and Bean 1993). Here, the vertices form exclusive groups and a tour has to contain exactly one vertex of each group. The standard TSP can be seen as a special instance of the generalized TSP, in which the size of each group is one. See figure 2 for a comparison of the two models. In our model, there is one group G_j per beam b_j and it contains one element per configuration in which b_j is feasible, i.e.

$$G_j = \{(b_j, c_k) : c_k \in F_j\}. \quad (7)$$

Thus, we have N groups with at least one and at most M vertices each which form the overall set of vertices

$$V_{GTSP} = \bigcup_{j \in \{1, \dots, N\}} G_j \quad (8)$$

with edges

$$E_{GTSP} = \{((b_i, c_k), (b_j, c_l)) : (b_i, c_k) \in G_i, (b_j, c_l) \in G_j, i \neq j\} \quad (9)$$

of our GTSP model. The size of the solution space depends on the sizes of the individual groups. The $(N - 1)!/2$ possible tours in terms of visiting each group in a sequence $(G^1, G^2, \dots, G^N, G^1)$ have to be multiplied by the product $\prod_j |G_j|$ of the number of vertices of each group. In the worst case with all groups containing M vertices, we end up with $(N - 1)!/2 \cdot M^N$ possible solutions.

While the GTSP provides a suitable model for our problem, finding its solution is typically hard. There exist algorithms to transform any GTSP to a symmetric standard TSP (Noon and Bean 1993) of similar size. However, this introduces very large costs on some of the edges and results in a TSP with structures which hamper state-of-the-art solvers. Some branch & cut algorithms for solving GTSPs exist (Fischetti *et al* 1997), but they are limited to very small problem instances. Hence, several heuristic solvers have been introduced, which do not guarantee optimality but are able to find good approximations in reasonable time. The GLKH solver (Helsgaun 2013) based on the Lin–Kernighan–Helsgaun heuristic (Lin and Kernighan 1973, Helsgaun 2009) has been shown to work well on GTPS problems (Helsgaun 2015). Other heuristic approaches include methods based on genetic algorithms (Gutin and Karapetyan 2010), ant-colony search (Jun-man and Yi 2012), or particle-swarm optimization (Shi *et al* 2007). Subsequently we present three methods to solve the GTPS including the US-robot. For comparison we also solve the TSP optimizing just the LINAC-robot motion without adding the US-robot.

2.2.3. Method A: LINAC-robot motion only

As a baseline we solve the TSP resulting from transforming the HPP to optimize the path of the LINAC-robot using Concorde (Applegate *et al* 2003). This solver is based on a mixed-integer programming (MIP) approach and employs efficient branch & cut strategies for TSP. Hence, the solver is complete and optimal and known to be very efficient, even in case of relatively large TSP instances. Solving the TSP results in a sequence S_A of beams which encodes the motion of the LINAC-robot.

2.2.4. Method B: decoupled, no-optimization

The solution to the TSP from method A can be extended in a GTPS solution in a straightforward fashion. We keep the same sequence S_A and start with an arbitrary US-robot configuration such that the first beam is feasible. Subsequently, the beams in the sequence are delivered until a beam is not feasible given the current US-robot configuration. In this case, the closest US-robot configuration is selected and the cost for the motion of both robots is considered.

As a post-processing step, we shift the resulting sequence S_B such that the last and first vertex are connected by the edge with highest weight. This weight does not contribute to the final costs as we are interested in a Hamiltonian path and not a tour.

2.2.5. Method C: decoupled, optimization

Although method B will always result in a feasible sequence of robot motion it may incur unnecessary cost as the configuration of the US-robot is considered at each beam delivery separately. This problem is tackled by our method C. In this approach, we again keep the beam sequence S_A from the problem without the US-robot fix. However, we now optimize the sequence of configurations. We do this by setting up a directed graph with artificial source and sink vertex as shown in figure 3. The source is connected by zero-weighted edges to all vertices containing the first beam in S_A . Likewise, all vertices containing the last beam in S_A are connected to the sink with zero costs. We now search for the shortest path from source to sink, which can be done by using Dijkstra's algorithm (Dijkstra 1959). This path is our resulting sequence S_B of beams and configurations. We apply the same post-processing as for method A, in order to remove the edge with largest cost from the costs of the sequence S_C .

2.2.6. Method D: combined, optimization

To obtain an estimate to what extent optimizing the full GTSP can improve the treatment time, we solve the problem using GLKH. We use its standard parameters and apply one run with 1000 iterations. For comparison, we also evaluate the influence of more iterations and restarts. As for all other methods, the highest edge of the tour is removed afterwards.

2.3. Case study

To illustrate the methods, we consider a prostate cancer scenario for which a previous plan quality analysis has shown that the effect of adding the US-robot can be mitigated by using multiple configurations (Gerlach *et al* 2017a, 2017b). Using the same constraints for inverse planning but different parameters for the robot configurations we now study to what extent the proposed methods can also mitigate the US-robot's effect with respect to treatment time. We apply the methods to 10 patient cases previously treated with the CyberKnife and having PTV sizes ranging from 52.7 cm³ to 115.4 cm³ with mean 84.5 cm³ and standard deviation 13.8 cm³.

2.3.1. Robot configurations

For each patient, a promising ultrasound probe pose was determined based on the results of the previous planning studies. Moreover, three different robot base positions around the patients were selected and are shown in figure 4(a). One robot base is located between the patients' legs and allows to vary the LIFT angle collision-freely within the interval $[-69^\circ, 69^\circ]$. For the two positions left of the patient, the intervals are $[-90^\circ, 90^\circ]$ and

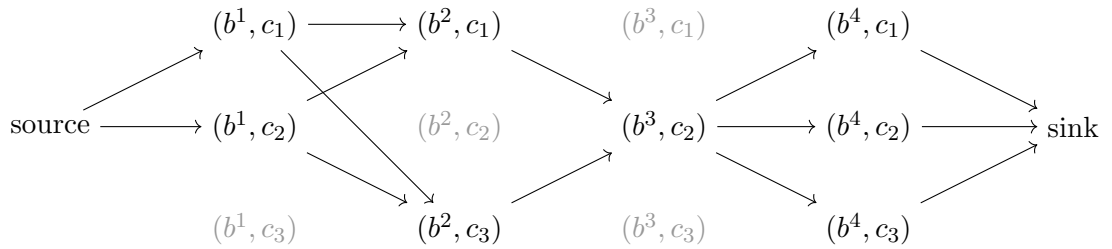


Figure 3. Illustration of method B for four beams and three configurations of the US-robot. Given the optimal beam sequence for the linear accelerator, i.e. b^i is the i th beam in the sequence, a directed graph is constructed. The shortest path from source to sink gives the best sequence of US-robot configurations under the fixed beam order. The costs of the edges are equal to those of the GTSP model. Infeasible combinations of beam and configurations are shown grayed out. Therefore, at least one configuration change (from c_1 to c_2) is required to deliver all beams in this example.

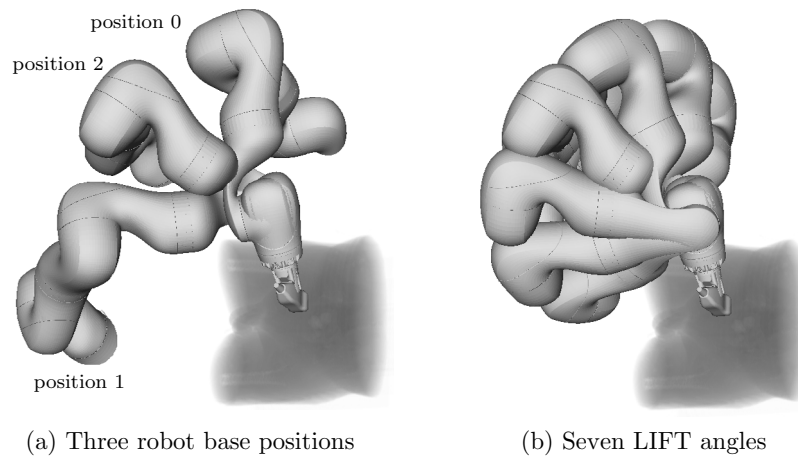


Figure 4. An overlaid visualization of the three robot positions around the patient which we consider (a). For position 2, an overlay of seven different configurations due to equidistantly spaced LIFT angles is shown (b).

$[-115^\circ, 115^\circ]$. During planning we consider using 3, 5, and 7 LIFT angles, which we select equidistantly in these intervals. For the base position with the widest range, the seven LIFT angles in use are illustrated in figure 4(b).

To investigate the effect of robot speed on treatment time, we assume 1%, 3%, 5%, and 10% for λ_{LA} and 1%, 4%, 7%, and 10% for λ_{US} . In the actual CyberKnife system, the linear accelerator is moved with approximately 3%–4% of the maximum speed in Cartesian space.

2.3.2. Treatment planning parameters

In our study, we are mainly interested in the effect different robot motion patterns have on treatment time. We adopt the same bounds as in the previous study (Gerlach *et al* 2017a), constraining the dose in PTV, rectum, and bladder to 4050 cGy, 3600 cGy, and 3600 cGy, respectively. SHELL structures are used to maintain the same level of conformality with patient-depending upper bounds from 2700 to 2975 cGy and from 3525 to 3660 cGy, respectively. The PTV has a target dose of 3625 cGy. For dose delivery, we assume a rate of 800 MU min^{-1} . The upper MU limit is set to 300 MU per beam and 40 000 MU in total. For each combination of patient and robot setting, 50 random sets of 6000 candidate beams are generated and used for treatment planning. In total, the delivery of 4500 different sets of candidate beams is analyzed for 12 different combinations of robot speeds.

The objective for the optimization is minimization of underdosage. This is formulated as a linear function by summing the difference to target dose over all voxels with a current dose below the target dose. Note that solving the optimization problem will result in many of the candidate beams having zero weight, i.e. they are not used for treatment. Only the beams having a positive weight are subsequently considered for optimizing the robot paths.

3. Results

Using multiple US-robot configurations during the treatment allows for more beam directions, because each beam only has to be feasible in at least one of the configurations. Table 1 shows that when 3 LIFT angles are considered, on average 4.1% of the sampled candidate beams are only feasible in one of the three configurations with an additional 16.1% being feasible in two configurations. The remaining 79.8% are feasible in all three

Table 1. Distribution of the number of US-robot configurations in which the beams are feasible for different numbers of LIFT angles. Columns labeled with *treatment* only consider beams having a non-zero weight after dose optimization, columns labeled with *candidates* consider all 6000 candidate beams.

# Feas	Feasible beams in % (mean and std)					
	3 LIFTs		5 LIFTs		7 LIFTs	
	Candidates	Treatment	Candidates	Treatment	Candidates	Treatment
1	4.1 ± 1.3	9.1 ± 3.7	1.0 ± 0.6	2.0 ± 1.1	0.6 ± 0.3	1.2 ± 0.9
2	16.1 ± 7.1	20.6 ± 4.4	3.5 ± 1.1	7.5 ± 2.7	1.4 ± 0.8	3.1 ± 2.0
3	79.8 ± 7.0	70.2 ± 3.3	6.5 ± 3.0	10.0 ± 2.3	2.8 ± 0.8	5.8 ± 1.6
4			11.7 ± 5.8	12.8 ± 3.5	3.9 ± 1.6	6.9 ± 1.9
5			77.3 ± 9.3	67.7 ± 4.2	6.9 ± 3.9	8.7 ± 2.9
6					7.8 ± 3.6	7.6 ± 2.2
7					76.6 ± 8.9	66.7 ± 3.6

configurations. Similarly, 77.3% and 76.6% are feasible in all configurations when 5 and 7 LIFT angles are used. If we only consider the treatment beams instead, the fraction of beams which are feasible in all configurations drops by about 10 percentage points to 67.7% and 66.7% for 5 and 7 LIFTs, respectively. Thus, beams which are not always feasible are disproportionately selected by the optimizer. The same holds for the case of 3 LIFT angles. If only the three patients with the smallest prostates are considered, the average percentage of treatment beams visible in all configurations are 69.5%, 66.7%, and 66.1% for 3, 5, and 7 LIFT angles, respectively. For the three patients with the largest prostates, these values are 71.6%, 69.5%, and 68.2%, respectively.

Figure 5 summarizes the results of the robot path optimization without consideration of the US-robot (method A). The median fraction of treatment time, i.e. time for beam delivery and the motion of linac, is 11.6% for $\lambda_{LA} = 3\%$ and 3.8% for $\lambda_{LA} = 10\%$. For the slow linac with $\lambda_{LA} = 1\%$ it increases to 28.3%. For comparison, results for a random trajectory are shown. Our simulated velocities are compared in figure 6 with velocities of the manipulator which were logged during two real CyberKnife treatments. Only traveling distances above 100 mm are considered in the histograms for both our simulation and the real data. This excludes situations in which not the maximum velocity but rather the feasible acceleration dominates the traveling time.

Considering the US-robot, generally its motion is related to an increase in the overall treatment time, i.e. time for beam delivery and robot motion. The results are presented in figure 7 for different combinations of robot speeds and different numbers of LIFT angles in use. The 100% reference is the overall time by method A, i.e. representing motion of the LINAC-robot only. The results for methods B, C, and D move towards 100% if the US-robot is considerably faster than the LINAC-robot, i.e. the overhead due to the US-robot vanishes. For the other extreme, i.e. when the LINAC-robot moves about ten times faster than the US-robot, the median increase in treatment time is approximately 20% and 10% for method B and D, respectively. For the realistic case of LINAC-robot and US-robot operating at 3% and 4% of their maximum speeds, respectively, the median increase is about 4%. More detailed results are shown in table 2, which compares only the times needed for moving the robots. The time for coordinated linac and US-robot motion by methods B, C, and D is expressed relative to the reference motion by method A. Method B is outperformed by methods C and D. Whether method C or D produces better results depends on the robot speed settings. The differences are mostly significant in terms of a Wilcoxon rank sum test. However, the variation of the results for method D is typically smaller than for method C.

Generally, the size of the PTV can have an impact on the treatment plan quality. To analyze the influence on our study, we grouped the three patients with the smallest PTVs (52.7, 67.1, and 70.3 cm³) and the three patients with the largest PTVs (93.2, 109.7, and 115.4 cm³). We use a Wilcoxon rank sum test to test the null hypothesis that the results for both groups are from distributions with equal median. As shown in table 3, significant differences are observed for most results of method D. For 31 of the 36 presented parameter combinations this hypothesis can be rejected on a 5% significance level.

Another potentially important parameter is the selected position of the US-robot's base. The individual results for the three positions in use are presented in table 4 together with pairwise p-values for the same statistical test as described before. The null hypothesis is rejected in 31 cases for position 0 and 1, in all 36 cases for position 1 and 2, and in 31 cases for position 0 and 2. The locations of the positions are illustrated in figure 4(a) and position 1 is the one between the legs of the patient. But note that also the feasible ranges of the LIFT angle are different for each position.

Method D uses the heuristic GTSP-solver GLKH. As for all iterative solvers, we can expect better solutions if we apply more iterations and restarts with different initial guesses. Figure 8 shows the relative improvements compared to our baseline settings. Note that these results are only based on a subset of our parameter combinations. Improvements up to 35% are observable in the diagrams. However, the GLKH runtime is basically linear

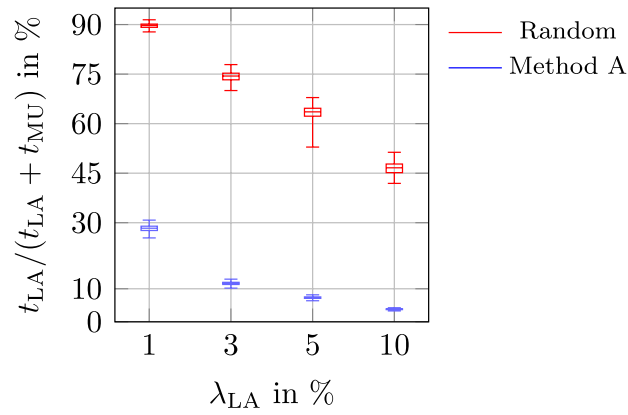
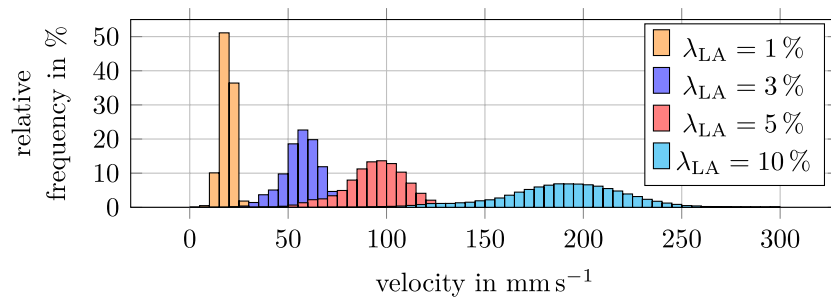
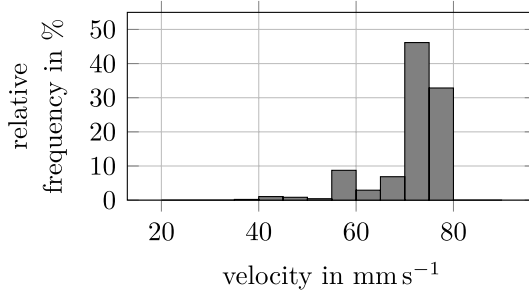


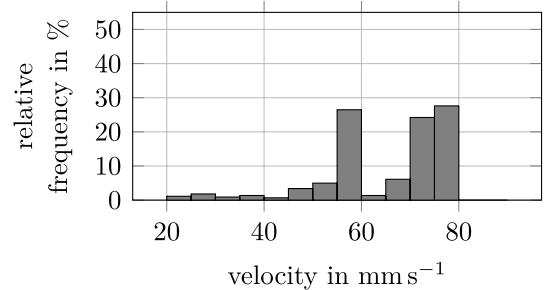
Figure 5. Contribution of the time for moving the LINAC-robot (t_{LA}) relative to the overall treatment time, i.e. time for robot motion and dose delivery ($t_{LA} + t_{MU}$). The velocity of the LINAC-robot is limited to different fractions (λ_{LA}) of its maximum joint velocities and the trajectories are calculated by method A (blue) and by selecting a random sequence of beams (red).



(a) Method A



(b) Real manipulator 1



(c) Real manipulator 2

Figure 6. Relative frequency of velocities for our simulations (a) and two real treatments (b) and (c). Only trajectories with an Euclidean distances above 100 mm are considered and the velocities are calculated with respect to Euclidean distance between the end positions and the total traveling time.

in number of iterations and restarts (if not calculated in parallel). Tripling the computation time by applying 3000 iterations led to an improvement of at most 6% in 90% of the cases. The same holds for tripling the time by applying 2 restarts.

Figure 9 compares the number of necessary configuration changes by the US-robot in the solutions of methods C and D. More configuration changes correspond to more robot motion close to the patient. The faster the robot with the linear accelerator moves, the clearer becomes the difference between the method. Method C is only able to optimize the sequence of US-robot configurations but uses a fixed sequence of beams. Method D optimizes both sequences and results in fewer changes of the configuration.

4. Discussion

We present methods to coordinate and optimize the motion of two robots in a scenario where one robot carries a linear accelerator to deliver beams of radiation and the second robot positions an ultrasound transducer for continuous image guidance. The LINAC-robot motion will always contribute to the overall treatment time if

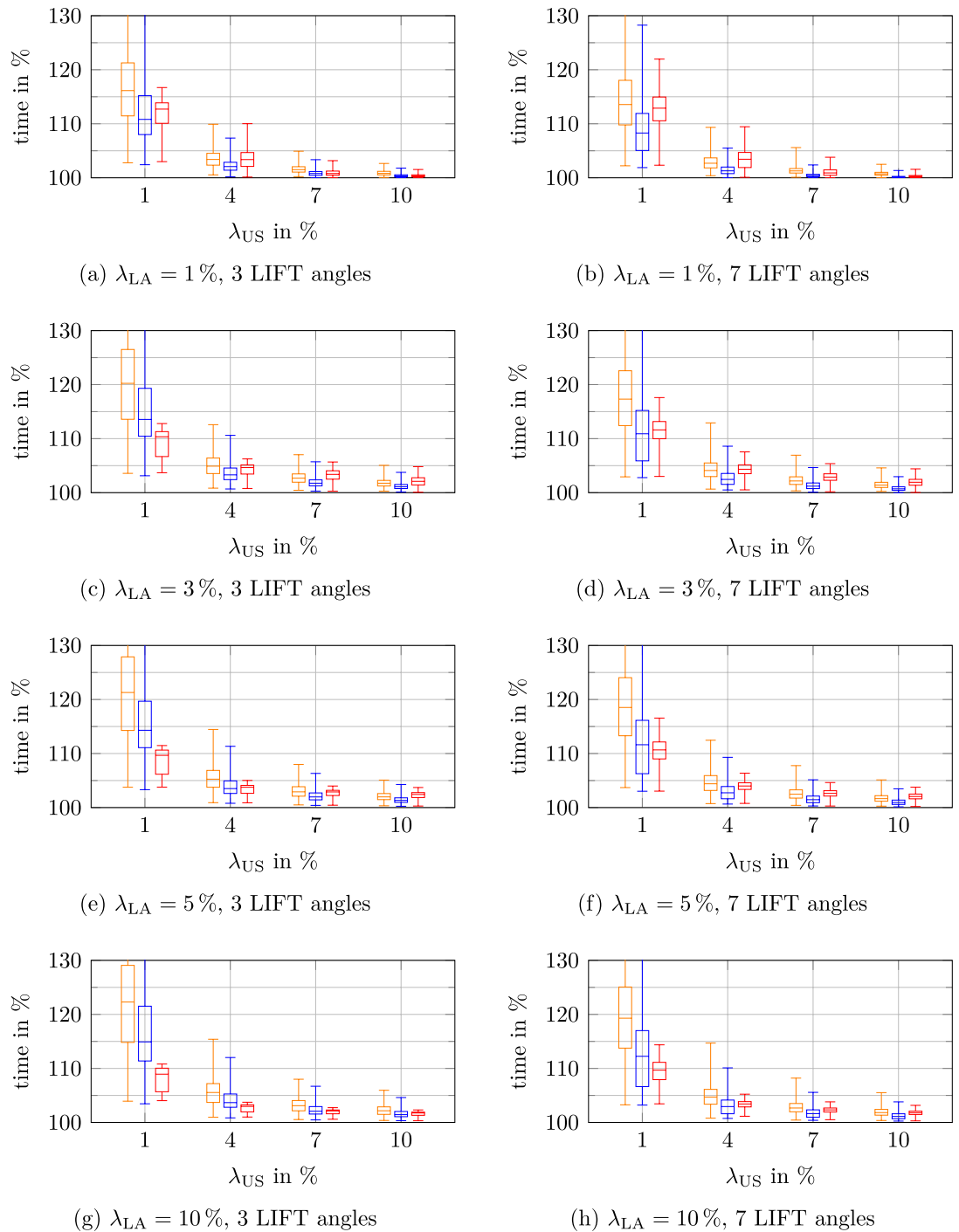


Figure 7. Relative overall treatment time, i.e. time for robot motion and beam delivery, when including of the US-robot by method B (orange), C (blue), and D (red). The results are shown for different percentages (λ_{LA} , λ_{US}) of the maximum joint velocities of the LINAC-robot and the US-robot as well as for 3 and 7 LIFT angles. The 100% baseline is the scenario without the US-robot and path planning for solely the LINAC-robot estimated by method A. Upper whiskers for $\lambda_{US} = 1\%$ are cut at 130%.

beams are delivered from different directions. Different approaches to optimize the path planning problem have been described (Dieterich and Gibbs 2011, Kearney *et al* 2018). We confirm that the TSP related to this problem (figure 5) can be very efficiently solved by state-of-the-art solvers. While the robot's travel time would depend on the desired velocity limits, these are typically far below the robot's specification and do not change, i.e. the same TSP solution would be valid even if the robot was moving twice as fast.

The CyberKnife M6 limits the end-effector velocity of its robot in Cartesian space to 60 mm s^{-1} or 80 mm s^{-1} , depending on the distance to certain obstacles. Instead, we limit the joint velocities in our simulations and therefore obtain differently shaped distributions for the velocities in Cartesian space (figure 6). However, the US-robot

Table 2. Mean μ and standard deviation σ of the time for robot motion by method B, C, and D (linac and US-robot motion) relative to method A (linac-only motion) for different combinations of LIFT angles and robot speeds. A Wilcoxon rank sum test is used to check the null hypothesis that two methods' results have equal median and the p-value is marked bold if it cannot be rejected on a 5% level.

#LIFTs	λ_{LA}	λ_{US}	Method B	Method C	Method D	$p_{B,C}$	$p_{B,D}$	$p_{C,D}$
3	1%	1%	$\mu = 1.60, \sigma = 0.25$	$\mu = 1.42, \sigma = 0.20$	$\mu = 1.42, \sigma = 0.10$	0.00	0.00	0.00
		4%	$\mu = 1.13, \sigma = 0.06$	$\mu = 1.08, \sigma = 0.04$	$\mu = 1.12, \sigma = 0.07$	0.00	0.21	0.00
		10%	$\mu = 1.03, \sigma = 0.02$	$\mu = 1.01, \sigma = 0.01$	$\mu = 1.01, \sigma = 0.01$	0.00	0.00	0.50
	3%	1%	$\mu = 2.79, \sigma = 0.78$	$\mu = 2.28, \sigma = 0.62$	$\mu = 1.81, \sigma = 0.20$	0.00	0.00	0.00
		4%	$\mu = 1.44, \sigma = 0.19$	$\mu = 1.31, \sigma = 0.15$	$\mu = 1.37, \sigma = 0.09$	0.00	0.00	0.00
		10%	$\mu = 1.16, \sigma = 0.07$	$\mu = 1.10, \sigma = 0.05$	$\mu = 1.18, \sigma = 0.08$	0.00	0.00	0.00
	5%	1%	$\mu = 4.00, \sigma = 1.31$	$\mu = 3.14, \sigma = 1.04$	$\mu = 2.20, \sigma = 0.30$	0.00	0.00	0.00
		4%	$\mu = 1.74, \sigma = 0.32$	$\mu = 1.52, \sigma = 0.25$	$\mu = 1.47, \sigma = 0.12$	0.00	0.00	0.00
		10%	$\mu = 1.28, \sigma = 0.12$	$\mu = 1.19, \sigma = 0.09$	$\mu = 1.31, \sigma = 0.09$	0.00	0.00	0.00
	10%	1%	$\mu = 7.02, \sigma = 2.67$	$\mu = 5.30, \sigma = 2.10$	$\mu = 3.16, \sigma = 0.56$	0.00	0.00	0.00
		4%	$\mu = 2.49, \sigma = 0.65$	$\mu = 2.07, \sigma = 0.52$	$\mu = 1.71, \sigma = 0.18$	0.00	0.00	0.00
		10%	$\mu = 1.59, \sigma = 0.25$	$\mu = 1.42, \sigma = 0.20$	$\mu = 1.43, \sigma = 0.10$	0.00	0.00	0.00
5	1%	1%	$\mu = 1.57, \sigma = 0.27$	$\mu = 1.40, \sigma = 0.20$	$\mu = 1.44, \sigma = 0.12$	0.00	0.00	0.00
		4%	$\mu = 1.11, \sigma = 0.06$	$\mu = 1.07, \sigma = 0.04$	$\mu = 1.11, \sigma = 0.06$	0.00	0.75	0.00
		10%	$\mu = 1.03, \sigma = 0.02$	$\mu = 1.01, \sigma = 0.01$	$\mu = 1.01, \sigma = 0.01$	0.00	0.00	0.00
	3%	1%	$\mu = 2.72, \sigma = 0.83$	$\mu = 2.23, \sigma = 0.63$	$\mu = 1.89, \sigma = 0.21$	0.00	0.00	0.00
		4%	$\mu = 1.42, \sigma = 0.20$	$\mu = 1.29, \sigma = 0.15$	$\mu = 1.38, \sigma = 0.11$	0.00	0.00	0.00
		10%	$\mu = 1.15, \sigma = 0.07$	$\mu = 1.09, \sigma = 0.05$	$\mu = 1.16, \sigma = 0.08$	0.00	0.00	0.00
	5%	1%	$\mu = 3.87, \sigma = 1.41$	$\mu = 3.07, \sigma = 1.07$	$\mu = 2.27, \sigma = 0.32$	0.00	0.00	0.00
		4%	$\mu = 1.71, \sigma = 0.33$	$\mu = 1.50, \sigma = 0.25$	$\mu = 1.53, \sigma = 0.13$	0.00	0.00	0.00
		10%	$\mu = 1.27, \sigma = 0.13$	$\mu = 1.18, \sigma = 0.09$	$\mu = 1.28, \sigma = 0.09$	0.00	0.00	0.00
	10%	1%	$\mu = 6.79, \sigma = 2.78$	$\mu = 5.16, \sigma = 2.16$	$\mu = 3.20, \sigma = 0.62$	0.00	0.00	0.00
		4%	$\mu = 2.43, \sigma = 0.68$	$\mu = 2.02, \sigma = 0.53$	$\mu = 1.80, \sigma = 0.19$	0.00	0.00	0.00
		10%	$\mu = 1.57, \sigma = 0.27$	$\mu = 1.40, \sigma = 0.20$	$\mu = 1.46, \sigma = 0.12$	0.00	0.00	0.00
	7	1%	$\mu = 1.51, \sigma = 0.22$	$\mu = 1.32, \sigma = 0.18$	$\mu = 1.45, \sigma = 0.11$	0.00	0.00	0.00
			$\mu = 1.10, \sigma = 0.05$	$\mu = 1.05, \sigma = 0.03$	$\mu = 1.12, \sigma = 0.06$	0.00	0.00	0.00
			$\mu = 1.03, \sigma = 0.01$	$\mu = 1.01, \sigma = 0.01$	$\mu = 1.01, \sigma = 0.01$	0.00	0.00	0.00
		3%	$\mu = 2.56, \sigma = 0.67$	$\mu = 2.00, \sigma = 0.56$	$\mu = 1.99, \sigma = 0.21$	0.00	0.00	0.00
			$\mu = 1.38, \sigma = 0.17$	$\mu = 1.23, \sigma = 0.13$	$\mu = 1.37, \sigma = 0.10$	0.00	0.03	0.00
			$\mu = 1.13, \sigma = 0.06$	$\mu = 1.07, \sigma = 0.04$	$\mu = 1.16, \sigma = 0.07$	0.00	0.00	0.00
		5%	$\mu = 3.64, \sigma = 1.14$	$\mu = 2.67, \sigma = 0.95$	$\mu = 2.44, \sigma = 0.32$	0.00	0.00	0.00
			$\mu = 1.64, \sigma = 0.28$	$\mu = 1.40, \sigma = 0.22$	$\mu = 1.54, \sigma = 0.12$	0.00	0.00	0.00
			$\mu = 1.24, \sigma = 0.11$	$\mu = 1.14, \sigma = 0.08$	$\mu = 1.28, \sigma = 0.08$	0.00	0.00	0.00
	10%	1%	$\mu = 6.31, \sigma = 2.31$	$\mu = 4.39, \sigma = 1.92$	$\mu = 3.50, \sigma = 0.58$	0.00	0.00	0.00
		4%	$\mu = 2.30, \sigma = 0.57$	$\mu = 1.83, \sigma = 0.47$	$\mu = 1.88, \sigma = 0.19$	0.00	0.00	0.00
		10%	$\mu = 1.51, \sigma = 0.22$	$\mu = 1.32, \sigma = 0.18$	$\mu = 1.47, \sigma = 0.11$	0.00	0.00	0.00

does not move its end-effector and therefore we chose to consistently control the joint velocities for both robots. The observed velocities in our simulations are roughly centered around 20, 60, 100, and 200 mm s⁻¹ which corresponds to 1%, 3%, 5%, and 10% of the maximum velocity in Euclidean space, which is 2 m s⁻¹.

Considering an actively moving US-robot in this setup allows for more feasible beam directions. Table 1 showed that inverse planning led to disproportionately many beams which are blocked in at least one of the considered US-robot configurations being used for treatment. However, the main purpose of our work is to study the impact that integrating an US-robot would have on the treatment time. If the US-robot is able to change its configuration in a shorter time than the LINAC-robot needs to move to deliver the next beam, then the total time for robot motion is the same as without the US-robot. However, this depends not only on the distance which

Table 3. Time for robot motion of method D (LINAC-robot and US-robot) relative to method A (only LINAC-robot) for the three patients with the smallest prostate volumes and the three patients with the largest prostate volumes. Additionally, the p-values for the null hypothesis that both results are samples from distributions with equal median (Wilcoxon rank sum test) are given for each combination of parameters. Values above 5% are marked bold.

#LIFTs	λ_{LA}	λ_{US}	small (3)	p	large (3)
3	1%	1%	$\mu = 1.394, \sigma = 0.111$	0.03	$\mu = 1.411, \sigma = 0.095$
		4%	$\mu = 1.084, \sigma = 0.050$	0.00	$\mu = 1.138, \sigma = 0.070$
		10%	$\mu = 1.010, \sigma = 0.006$	0.00	$\mu = 1.014, \sigma = 0.010$
	3%	1%	$\mu = 1.768, \sigma = 0.220$	0.09	$\mu = 1.807, \sigma = 0.191$
		4%	$\mu = 1.344, \sigma = 0.103$	0.00	$\mu = 1.370, \sigma = 0.088$
		10%	$\mu = 1.136, \sigma = 0.078$	0.00	$\mu = 1.192, \sigma = 0.086$
	5%	1%	$\mu = 2.159, \sigma = 0.327$	0.88	$\mu = 2.184, \sigma = 0.294$
		4%	$\mu = 1.445, \sigma = 0.132$	0.01	$\mu = 1.470, \sigma = 0.113$
		10%	$\mu = 1.287, \sigma = 0.092$	0.00	$\mu = 1.314, \sigma = 0.084$
	10%	1%	$\mu = 3.096, \sigma = 0.599$	0.49	$\mu = 3.143, \sigma = 0.544$
		4%	$\mu = 1.684, \sigma = 0.191$	0.53	$\mu = 1.700, \sigma = 0.176$
		10%	$\mu = 1.410, \sigma = 0.111$	0.10	$\mu = 1.423, \sigma = 0.102$
5	1%	1%	$\mu = 1.398, \sigma = 0.115$	0.00	$\mu = 1.448, \sigma = 0.105$
		4%	$\mu = 1.084, \sigma = 0.051$	0.00	$\mu = 1.125, \sigma = 0.061$
		10%	$\mu = 1.007, \sigma = 0.006$	0.00	$\mu = 1.012, \sigma = 0.008$
	3%	1%	$\mu = 1.829, \sigma = 0.207$	0.00	$\mu = 1.901, \sigma = 0.198$
		4%	$\mu = 1.340, \sigma = 0.100$	0.00	$\mu = 1.380, \sigma = 0.106$
		10%	$\mu = 1.123, \sigma = 0.066$	0.00	$\mu = 1.167, \sigma = 0.074$
	5%	1%	$\mu = 2.190, \sigma = 0.293$	0.00	$\mu = 2.259, \sigma = 0.300$
		4%	$\mu = 1.480, \sigma = 0.125$	0.00	$\mu = 1.535, \sigma = 0.123$
		10%	$\mu = 1.248, \sigma = 0.089$	0.00	$\mu = 1.293, \sigma = 0.090$
	10%	1%	$\mu = 3.030, \sigma = 0.571$	0.00	$\mu = 3.170, \sigma = 0.579$
		4%	$\mu = 1.737, \sigma = 0.178$	0.00	$\mu = 1.803, \sigma = 0.171$
		10%	$\mu = 1.418, \sigma = 0.116$	0.00	$\mu = 1.465, \sigma = 0.112$
7	1%	1%	$\mu = 1.427, \sigma = 0.109$	0.00	$\mu = 1.457, \sigma = 0.107$
		4%	$\mu = 1.097, \sigma = 0.057$	0.00	$\mu = 1.126, \sigma = 0.059$
		10%	$\mu = 1.008, \sigma = 0.007$	0.00	$\mu = 1.011, \sigma = 0.009$
	3%	1%	$\mu = 1.928, \sigma = 0.209$	0.00	$\mu = 2.000, \sigma = 0.209$
		4%	$\mu = 1.339, \sigma = 0.093$	0.00	$\mu = 1.378, \sigma = 0.104$
		10%	$\mu = 1.140, \sigma = 0.066$	0.00	$\mu = 1.167, \sigma = 0.067$
	5%	1%	$\mu = 2.348, \sigma = 0.334$	0.00	$\mu = 2.447, \sigma = 0.311$
		4%	$\mu = 1.506, \sigma = 0.122$	0.00	$\mu = 1.546, \sigma = 0.126$
		10%	$\mu = 1.254, \sigma = 0.083$	0.00	$\mu = 1.281, \sigma = 0.085$
	10%	1%	$\mu = 3.383, \sigma = 0.577$	0.03	$\mu = 3.481, \sigma = 0.576$
		4%	$\mu = 1.834, \sigma = 0.195$	0.00	$\mu = 1.895, \sigma = 0.181$
		10%	$\mu = 1.436, \sigma = 0.112$	0.00	$\mu = 1.471, \sigma = 0.115$

each robot has to travel but also on their speeds. The results in figure 7 and table 2 illustrate that a combination of a 1% LINAC-robot speed and 10% US-robot speed would indeed result in a negligible increase in travel time of approximately 1%. In practice, the speed of the robotic CyberKnife is limited to at most 4% of the maximum robot speed (figures 6(b) and (c)). Considering $\lambda_{LA} = 3\%$ and a similarly conservative motion setting of 4% of maximum speed for the US-robot, we get an increase in travel time in the order of 30%. This can be explained by the fact that the US-robot sometimes has to move its elbow substantially to avoid beam blocking. For all methods and numbers of LIFT angles in figure 7, the additional robot motion corresponds to a median increase of the overall time by less than 5%. However, it is important to note that for x-ray-based image-guided treatments the linac also needs to move out of the x-ray beam path. Thus, our solution from method A had to be corrected by the time needed for these movements as well, if the current clinical setup with x-ray imaging is considered. Additionally, the x-ray imaging is limited to the time when the linac does not block the beam path. Instead, our setup allows for continuous imaging and tracking. This is especially an advantage if spontaneous motions of the organs

Table 4. Results of method D relative to method A (no US-robot) for each robot base position separately. Additionally, the p-values for the null hypothesis that both results are samples from distributions with equal median (Wilcoxon rank sum test) are given for each combination of parameters. Values above 5% are marked bold.

#LIFTs	λ_{LA}	λ_{US}	robot 0	$p_{0,1}$	robot 1	$p_{1,2}$	robot 2	$p_{2,0}$
3	1%	1%	$\mu = 1.39, \sigma = 0.10$	0.65	$\mu = 1.39, \sigma = 0.11$	0.00	$\mu = 1.47, \sigma = 0.06$	0.000
		4%	$\mu = 1.10, \sigma = 0.05$	0.00	$\mu = 1.13, \sigma = 0.08$	0.04	$\mu = 1.13, \sigma = 0.07$	0.000
		10%	$\mu = 1.01, \sigma = 0.01$	0.00	$\mu = 1.02, \sigma = 0.01$	0.00	$\mu = 1.01, \sigma = 0.01$	0.000
	3%	1%	$\mu = 1.73, \sigma = 0.19$	0.00	$\mu = 1.76, \sigma = 0.22$	0.00	$\mu = 1.93, \sigma = 0.11$	0.000
		4%	$\mu = 1.35, \sigma = 0.10$	0.81	$\mu = 1.34, \sigma = 0.10$	0.00	$\mu = 1.42, \sigma = 0.06$	0.000
		10%	$\mu = 1.16, \sigma = 0.07$	0.00	$\mu = 1.18, \sigma = 0.09$	0.00	$\mu = 1.20, \sigma = 0.08$	0.000
	5%	1%	$\mu = 2.07, \sigma = 0.27$	0.00	$\mu = 2.13, \sigma = 0.34$	0.00	$\mu = 2.40, \sigma = 0.15$	0.000
		4%	$\mu = 1.45, \sigma = 0.11$	0.95	$\mu = 1.43, \sigma = 0.13$	0.00	$\mu = 1.53, \sigma = 0.08$	0.000
		10%	$\mu = 1.29, \sigma = 0.08$	0.44	$\mu = 1.29, \sigma = 0.10$	0.00	$\mu = 1.35, \sigma = 0.06$	0.000
	10%	1%	$\mu = 2.90, \sigma = 0.49$	0.00	$\mu = 3.07, \sigma = 0.61$	0.00	$\mu = 3.52, \sigma = 0.33$	0.000
		4%	$\mu = 1.65, \sigma = 0.17$	0.00	$\mu = 1.66, \sigma = 0.20$	0.00	$\mu = 1.83, \sigma = 0.10$	0.000
		10%	$\mu = 1.41, \sigma = 0.10$	0.26	$\mu = 1.39, \sigma = 0.12$	0.00	$\mu = 1.49, \sigma = 0.07$	0.000
5	1%	1%	$\mu = 1.46, \sigma = 0.10$	0.00	$\mu = 1.38, \sigma = 0.10$	0.00	$\mu = 1.49, \sigma = 0.12$	0.000
		4%	$\mu = 1.12, \sigma = 0.06$	0.00	$\mu = 1.08, \sigma = 0.05$	0.00	$\mu = 1.14, \sigma = 0.06$	0.000
		10%	$\mu = 1.01, \sigma = 0.01$	0.00	$\mu = 1.01, \sigma = 0.01$	0.00	$\mu = 1.01, \sigma = 0.01$	0.077
	3%	1%	$\mu = 1.92, \sigma = 0.17$	0.00	$\mu = 1.80, \sigma = 0.19$	0.00	$\mu = 1.97, \sigma = 0.23$	0.000
		4%	$\mu = 1.38, \sigma = 0.09$	0.00	$\mu = 1.32, \sigma = 0.09$	0.00	$\mu = 1.43, \sigma = 0.10$	0.000
		10%	$\mu = 1.16, \sigma = 0.06$	0.00	$\mu = 1.12, \sigma = 0.07$	0.00	$\mu = 1.19, \sigma = 0.07$	0.000
	5%	1%	$\mu = 2.29, \sigma = 0.24$	0.00	$\mu = 2.11, \sigma = 0.28$	0.00	$\mu = 2.41, \sigma = 0.34$	0.000
		4%	$\mu = 1.55, \sigma = 0.11$	0.00	$\mu = 1.47, \sigma = 0.12$	0.00	$\mu = 1.57, \sigma = 0.14$	0.000
		10%	$\mu = 1.29, \sigma = 0.07$	0.00	$\mu = 1.23, \sigma = 0.08$	0.00	$\mu = 1.33, \sigma = 0.09$	0.000
	10%	1%	$\mu = 3.22, \sigma = 0.47$	0.00	$\mu = 2.86, \sigma = 0.55$	0.00	$\mu = 3.52, \sigma = 0.63$	0.000
		4%	$\mu = 1.83, \sigma = 0.15$	0.00	$\mu = 1.72, \sigma = 0.17$	0.00	$\mu = 1.86, \sigma = 0.21$	0.001
		10%	$\mu = 1.47, \sigma = 0.10$	0.00	$\mu = 1.40, \sigma = 0.11$	0.00	$\mu = 1.51, \sigma = 0.13$	0.000
7	1%	1%	$\mu = 1.42, \sigma = 0.09$	0.00	$\mu = 1.50, \sigma = 0.08$	0.00	$\mu = 1.43, \sigma = 0.13$	0.175
		4%	$\mu = 1.12, \sigma = 0.06$	0.00	$\mu = 1.14, \sigma = 0.06$	0.00	$\mu = 1.10, \sigma = 0.06$	0.000
		10%	$\mu = 1.01, \sigma = 0.01$	0.00	$\mu = 1.01, \sigma = 0.01$	0.00	$\mu = 1.01, \sigma = 0.01$	0.000
	3%	1%	$\mu = 1.98, \sigma = 0.16$	0.00	$\mu = 2.07, \sigma = 0.14$	0.00	$\mu = 1.93, \sigma = 0.27$	0.000
		4%	$\mu = 1.34, \sigma = 0.07$	0.00	$\mu = 1.41, \sigma = 0.08$	0.00	$\mu = 1.36, \sigma = 0.11$	0.001
		10%	$\mu = 1.16, \sigma = 0.06$	0.01	$\mu = 1.17, \sigma = 0.06$	0.00	$\mu = 1.15, \sigma = 0.07$	0.000
	5%	1%	$\mu = 2.40, \sigma = 0.24$	0.00	$\mu = 2.55, \sigma = 0.22$	0.00	$\mu = 2.37, \sigma = 0.43$	0.029
		4%	$\mu = 1.51, \sigma = 0.10$	0.00	$\mu = 1.58, \sigma = 0.10$	0.00	$\mu = 1.53, \sigma = 0.15$	0.047
		10%	$\mu = 1.26, \sigma = 0.07$	0.00	$\mu = 1.32, \sigma = 0.08$	0.00	$\mu = 1.26, \sigma = 0.09$	0.932
	10%	1%	$\mu = 3.40, \sigma = 0.45$	0.00	$\mu = 3.71, \sigma = 0.42$	0.00	$\mu = 3.39, \sigma = 0.75$	0.204
		4%	$\mu = 1.88, \sigma = 0.14$	0.00	$\mu = 1.95, \sigma = 0.13$	0.00	$\mu = 1.81, \sigma = 0.25$	0.000
		10%	$\mu = 1.44, \sigma = 0.09$	0.00	$\mu = 1.51, \sigma = 0.09$	0.00	$\mu = 1.45, \sigma = 0.14$	0.129

occur, because these would not be detected until the next x-ray images are acquired and thereby corrupt the actually achieved dose distribution.

Comparing the results for method B to the results for methods C and D (figure 7), it is clear that simply using the same beam sequence as without the US-robot is not optimal. Interestingly, the GTSP instances resulting from an inclusion of the US-robot motion are no longer solvable exactly in a reasonable amount of time. Both methods C and D employ heuristics and generally there is no guarantee to find a global optimum. While method D employs a more sophisticated heuristic included in the GLKH solver, it does not always result in the shortest motion. Particularly when the speed of the LINAC-robot is low, our proposed heuristic C compares favorably. This is remarkable, as method C is both deterministic and substantially faster than method D. The computation time for the baseline GLKH version with 1000 iterations and no restart is already in the order of 1 h compared to few seconds for method C (including solving the TSP). However, in a clinical setting the allowed velocity of the US-robot will be limited. For the cases with the US-robot being slower than the LINAC-robot, method D is able to further improve the solution in most situations, except when a large number of LIFT angles is considered.

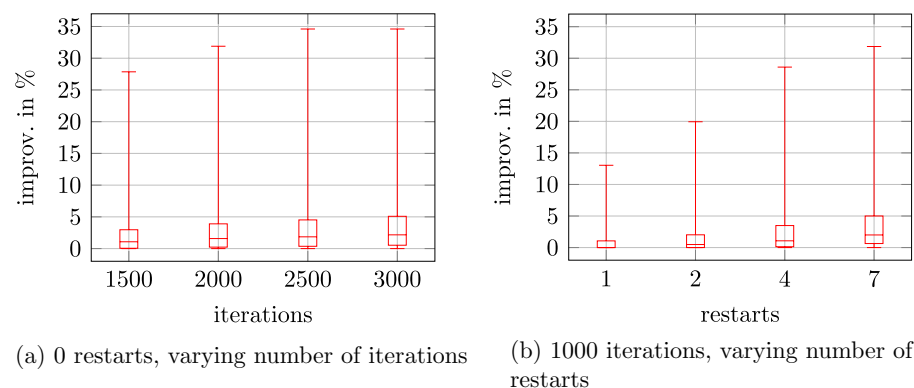


Figure 8. Percentual reduction of the time for robot motion if using more than 1000 iterations (a) or if using restarts (b) of GLKH (used in method D). Data of each number of restarts are based on 160 scenarios. For the varying number of iterations, additionally 8 runs have been evaluated for each scenario.

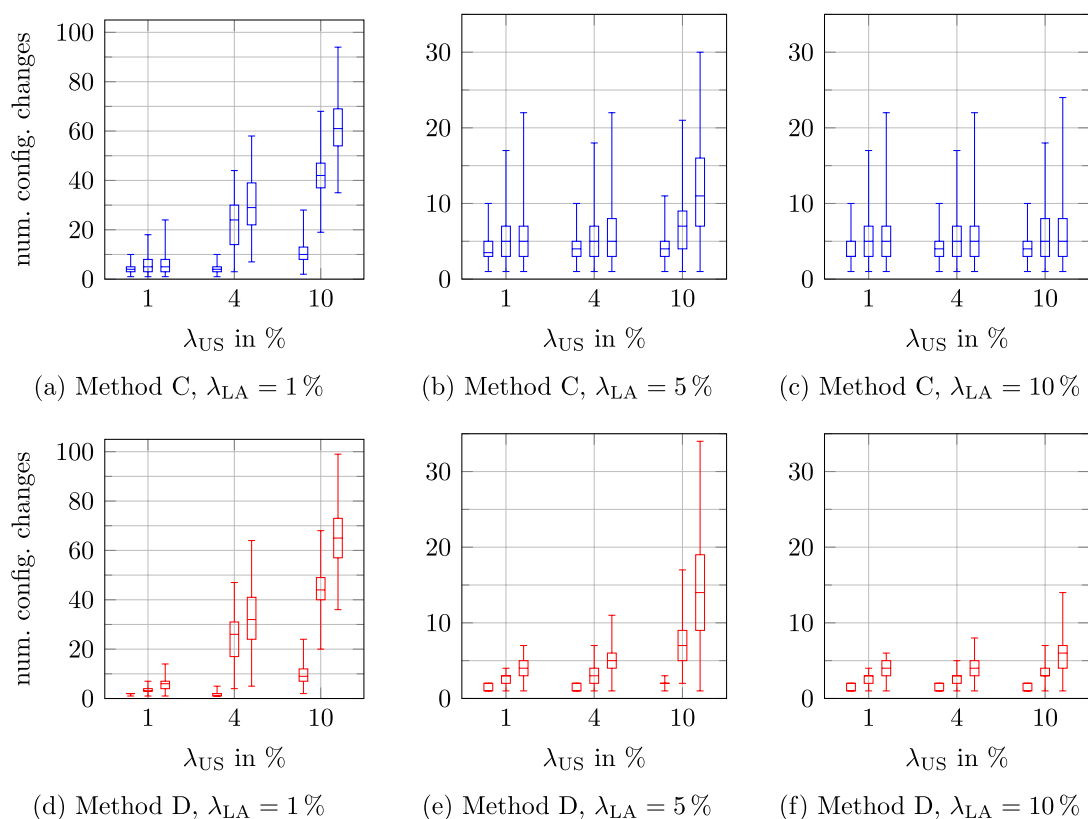


Figure 9. Number of configuration changes of the US-robot during the treatment. Upper row (blue) shows beam sequences determined by method C for different speeds of the linear accelerator, lower row (red) by method D. For each speed of the US-robot, results for 3, 5, and 7 LIFT angles are presented (left to right at each λ_{US} tick).

The quality of the solutions by method D can be further improved in general by increasing the number of iterations and restarts (figure 8), but this comes with very high costs in terms of additional computational time. However, method D often gives solutions with fewer configuration changes for the US-robot, i.e. motion close to the patient, compared to method C (figure 9). Note that if the linac is moved slowly, the US-robot will still change its configuration more than 50 times.

Our analysis also indicates that the US-robot's placement has an impact on the total travel time. We mostly observed significant deviations of the medians for the three robot setups under consideration (table 4). Similarly, the results for patients with a small prostate and patients with a large prostate showed significant deviations (table 3). For the large prostates a higher temporal overhead was observed.

While approaches to minimize the impact of intra-fractional ultrasound imaging have been proposed, they typically come with some limitations, too. The Clarity system (Elekta) is used for setup and motion detection

during radiation therapy of the prostate (Abramowitz *et al* 2012, Western *et al* 2015, Grimwood *et al* 2018). The system uses a transperineal approach and is thus limited to a relatively small volume. Another approach is to construct the ultrasound transducer such that beams can pass without substantial attenuation (Schlosser and Hristov 2016). However, the design does not include the robotic arm and the CyberKnife's relative beam motion due to active motion compensation may complicate dose calculations accounting for any residual attenuation. In contrast, we have demonstrated that using a commercial 7-DoF robotic arm and coordinating the motion of both robots allows for practical treatment times.

So far, configuration changes by the US-robot are only considered between delivered beams. Instead, one could also consider to move the US-robot during beam delivery to further decrease the overhead of its motion. However, separate motion and beam delivery might be more realistic in terms of safety, because it allows to check beam-wise for a conflict between the beam and the US-robot configuration. Otherwise, a fine-grained evaluation of the whole trajectory might be required. Further improvements may also be possible by allowing arbitrary LIFT angles, which would potentially reduce the amount of motion until subsequent beams can be delivered.

5. Conclusion

Robotic ultrasound guidance in radiation therapy is a promising approach to realize non-invasive and non-ionizing real-time tracking of the motion and deformation of the target and surrounding structures. Using a kinematically redundant robot carrying the ultrasound probe, the effect of beam blocking can be largely mitigated. We study methods to also account for the potential prolongation of the treatment delivery due to configuration changes of the ultrasound robot. While we illustrate that the optimization problem to coordinate robotic beam delivery and robotic ultrasound is hard, we also show that practical solutions can be obtained with the proposed methods. We also demonstrate that the effect of robot coordination depends on the speed settings, the ultrasound robot's base position, and the target size. Considering that continuous ultrasound motion monitoring would be particularly helpful to detect spontaneous motion in the abdomen, the relatively small overhead in treatment time of less than 4% would be acceptable.

Acknowledgments

This work was partially funded by Deutsche Forschungsgemeinschaft (Grant SCHL 1844/3-1).

References

- Abramowitz M, Bossart E, Flook R, Wu X, Brooks R, Lachaine M, Lathuiliere F and Pollack A 2012 Noninvasive real-time prostate tracking using a transperineal ultrasound approach *Int. J. Radiat. Oncol. Biol. Phys.* **84** S133
- Applegate D, Bixby R, Chvatal V and Cook W 2003 Concorde TSP solver 03.12.19 (<http://math.uwaterloo.ca/tsp/concorde/>)
- Bazalova-Carter M, Schlosser J, Chen J and Hristov D 2015 Monte Carlo modeling of ultrasound probes for image guided radiotherapy *Med. Phys.* **42** 5745–56
- Bell M A L, Sen H T, Iordachita I I, Kazanzides P and Wong J 2014 *In vivo* reproducibility of robotic probe placement for a novel ultrasound-guided radiation therapy system *J. Med. Imaging* **1** 025001
- Beltran C, Herman M G and Davis B J 2008 Planning target margin calculations for prostate radiotherapy based on intrafraction and interfraction motion using four localization methods *Int. J. Radiat. Oncol. Biol. Phys.* **70** 289–95
- Camps S M, Fontanarosa D, de With P H N, Verhaegen F and Vanneste B G L 2018 The use of ultrasound imaging in the external beam radiotherapy workflow of prostate cancer patients *Biomed. Res. Int.* **2018** 1–16
- De Luca V *et al* 2018 Evaluation of 2D and 3D ultrasound tracking algorithms and impact on ultrasound-guided liver radiotherapy margins *Med. Phys.* **45** 4986–5003
- Dieterich S and Gibbs I C 2011 The cyberknife in clinical use: current roles, future expectations *Front. Radiat. Ther. Oncol.* **43** 181–94 (IMRT, IGRT, SBRT—Advances in the Treatment Planning and Delivery of Radiotherapy)
- Dijkstra E W 1959 A note on two problems in connexion with graphs *Numer. Math.* **1** 269–71
- Dürichen R, Wissel T, Ernst F, Schlaefler A and Schweikard A 2014 Multivariate respiratory motion prediction *Phys. Med. Biol.* **59** 6043–60
- Echner G G *et al* 2009 The design, physical properties and clinical utility of an iris collimator for robotic radiosurgery *Phys. Med. Biol.* **54** 5359
- Fischetti M, Salazar González J J and Toth P 1997 A branch-and-cut algorithm for the symmetric generalized traveling salesman problem *Oper. Res.* **45** 378–94
- Fürweger C, Prins P, Coskan H and Heijmen B J 2016 Characteristics and performance of the first commercial multileaf collimator for a robotic radiosurgery system *Med. Phys.* **43** 2063–71
- Gerlach S, Kuhlmann I, Ernst F, Fürweger C and Schlaefler A 2017a Impact of robotic ultrasound image guidance on plan quality in SBRT of the prostate *Br. J. Radiol.* **90** 20160926
- Gerlach S, Kuhlmann I, Jauer P, Bruder R, Ernst F, Fürweger C and Schlaefler A 2017b Robotic ultrasound-guided SBRT of the prostate: feasibility with respect to plan quality *Int. J. Comput. Assist. Radiol. Surg.* **12** 149–59
- Grimwood A, McNair H A, O'Shea T P, Gilroy S, Thomas K, Bamber J C, Tree A C and Harris E J 2018 *In vivo* validation of Elekta's Clarity autoscans for ultrasound-based intrafraction motion estimation of the prostate during radiation therapy *Int. J. Radiat. Oncol. Biol. Phys.* **102** 912–21
- Gutin G and Karapetyan D 2010 A memetic algorithm for the generalized traveling salesman problem *Nat. Comput.* **9** 47–60
- Helsgaun K 2009 General k-opt submoves for the Lin–Kernighan TSP heuristic *Math. Program. Comput.* **1** 119–63

- Helsgaun K 2013 GLKH 1.0 (www.akira.ruc.dk/~keld/research/GLKH/)
- Helsgaun K 2015 Solving the equality generalized traveling salesman problem using the Lin–Kernighan–Helsgaun algorithm *Math. Program. Comput.* **7** 269–87
- Hossain S, Xia P, Huang K, Descovich M, Chuang C, Gottschalk A R, Roach M and Ma L 2010 Dose gradient near target-normal structure interface for nonisocentric cyberknife and isocentric intensity-modulated body radiotherapy for prostate cancer *Int. J. Radiat. Oncol. Biol. Phys.* **78** 58–63
- Ipsen S, Bruder R, O'Brien R, Keall P J, Schweikard A and Poulsen P R 2016 Online 4D ultrasound guidance for real-time motion compensation by MLC tracking *Med. Phys.* **43** 5695–704
- Jun-Man K and Yi Z 2012 Application of an improved ant colony optimization on generalized traveling salesman problem *Energy Procedia* **17** 319–25
- Jung J, Song S Y, Yoon S M, Kwak J, Yoon K, Choi W, Jeong S Y, Choi E K and Cho B 2015 Verification of accuracy of cyberknife tumor-tracking radiation therapy using patient-specific lung phantoms *Int. J. Radiat. Oncol. Biol. Phys.* **92** 745–53
- Kearney V, Cheung J P, McGuinness C and Solberg T D 2017 Cyberarc: a non-coplanar-arc optimization algorithm for cyberknife *Phys. Med. Biol.* **62** 5777
- Kearney V, Descovich M, Sudhyadhom A, Cheung J P, McGuinness C and Solberg T D 2018 A continuous arc delivery optimization algorithm for cyberknife M6 *Med. Phys.* **45** 3861–70
- Krauss A, Fast M F, Nill S and Oelfke U 2012 Multileaf collimator tracking integrated with a novel x-ray imaging system and external surrogate monitoring *Phys. Med. Biol.* **57** 2425
- Kuhlemann I, Schweikard A, Jauer P and Ernst F 2016 Robust inverse kinematics by configuration control for redundant manipulators with seven dof *IEEE Int. Conf. on Control, Automation and Robotics* pp 49–55
- Li M, Ballhausen H, Hegemann N S, Ganswindt U, Manapov F, Tritschler S, Roosen A, Gratzke C, Reiner M and Belka C 2015 A comparative assessment of prostate positioning guided by three-dimensional ultrasound and cone beam CT *Radiat. Oncol.* **10** 82
- Lin S and Kernighan B W 1973 An effective heuristic algorithm for the traveling-salesman problem *Oper. Res.* **21** 498–516
- McGuinness C M, Gottschalk A R, Lessard E, Nakamura J L, Pinnaduwa D, Pouliot J, Sims C and Descovich M 2015 Investigating the clinical advantages of a robotic linac equipped with a multileaf collimator in the treatment of brain and prostate cancer patients *J. Appl. Clin. Med. Phys.* **16** 284–95
- Nguyen D T, Bertholet J, Kim J, O'Brien R, Booth J T, Poulsen P R and Keall P J 2017 An interdimensional correlation framework for real-time estimation of six degree of freedom target motion using a single x-ray imager during radiotherapy *Phys. Med. Biol.* **63** 015010
- Noon C and Bean J 1993 An efficient transformation of the generalized traveling salesman problem *INFOR: Inf. Syst. Oper. Res.* **31** 39–44
- O'Shea T P, Garcia L J, Rosser K E, Harris E J, Evans P M and Bamber J C 2014 4D ultrasound speckle tracking of intra-fraction prostate motion: a phantom-based comparison with x-ray fiducial tracking using CyberKnife *Phys. Med. Biol.* **59** 1701–20
- Priester A M, Natarajan S and Culjat M O 2013 Robotic ultrasound systems in medicine *IEEE Trans. Ultrason. Ferroelectr. Freq. Control* **60** 507–23
- Ricotti R et al 2018 Evaluation of target coverage and margins adequacy during cyberknife lung optimized treatment *Med. Phys.* **45** 1360–8
- Antoni S-T, Rinast J, Ma X, Schupp S and Schlaefer A 2016 Online model checking for monitoring surrogate-based respiratory motion tracking in radiation therapy *Int. J. Comput. Assist. Radiol. Surg.* **11** 2085–96
- Schlaefer A and Schweikard A 2008 Stepwise multi-criteria optimization for robotic radiosurgery *Med. Phys.* **35** 2094–103
- Schlaefer A, Violette T, Muacevic A and Fürweger C 2013 Multicriteria optimization of the spatial dose distribution *Med. Phys.* **40** 121720
- Schlösser J and Hristov D 2016 Radiolucent 4D ultrasound imaging: system design and application to radiotherapy guidance *IEEE Trans. Med. Imaging* **35** 2292–300
- Schlösser J, Gong R H, Bruder R, Schweikard A, Jang S, Henrie J, Kamaya A, Koong A C, Chang D T and Hristov D 2016 Robotic intrafractional us guidance for liver SABR: system design, beam avoidance, and clinical imaging *Med. Phys.* **43** 5951–63
- Schlüter M, Gerlach S, Fürweger C and Schlaefer A 2019 Analysis and optimization of the robot setup for robotic-ultrasound-guided radiation therapy *Int. J. Comput. Assist. Radiol. Surg.* **14** 1379–87
- Schwaab J, Prall M, Sarti C, Kaderka R, Bert C, Kurz C, Parodi K, Guenther M and Jenne J E 2014 Ultrasound tracking for intra-fractional motion compensation in radiation therapy *Phys. Med.* **30** 578–82
- Şen H T, Bell M A L, Zhang Y, Ding K, Boctor E, Wong J, Iordachita I and Kazanzides P 2017 System integration and *in vivo* testing of a robot for ultrasound guidance and monitoring during radiotherapy *IEEE Trans. Biomed. Eng.* **64** 1608–18
- Shi X, Liang Y, Lee H, Lu C and Wang Q 2007 Particle swarm optimization-based algorithms for TSP and generalized TSP *Inf. Process. Lett.* **103** 16–176
- Western C, Hristov D and Schlösser J 2015 Ultrasound imaging in radiation therapy: from interfractional to intrafractional guidance *Cureus* **7** e280
- Yang Z Y, Chang Y, Liu H Y, Liu G and Li Q 2017 Target margin design for real-time lung tumor tracking stereotactic body radiation therapy using cyberknife xsight lung tracking system *Sci. Rep.* **7** 10826